Robust Control Scheme for Three-Phase Grid-Connected Inverters With *LCL*-Filter Under Unbalanced and Distorted Grid Conditions

Ngoc-Bao Lai, *Student Member, IEEE* and Kyeong-Hwa Kim, *Member, IEEE*

***Abstract*—The grid voltage, especially under unbalanced and harmonically distorted grid conditions, often distorts the injected currents of grid-connected inverters. To address this problem, a robust control scheme of grid-connected inverters is presented in this paper. The proposed scheme is achieved by an internal model (IM)-based current controller and a robust phase-locked loop (PLL) scheme. The robust PLL scheme employs open-loop filtering technique to offer exact steady-state performance as well as fast transient response. The IM-based current controller is stabilized using the linear matrix inequality approach to optimize the feedback gains, and implemented in the synchronous reference frame to reduce computational efforts. A state estimator is also introduced into current controller for the purpose of reducing the number of current sensors, which are often required in state feedback controller to damp the unstable dynamics of *LCL* filters. The validity of the proposed control scheme is demonstrated through comparative simulations and experimental results using a prototype grid-connected inverter.**

***Index Terms*—Grid-connected inverter, internal model principle, moving average filter, phase-locked loop, unbalanced and distorted grid.**

I. Introduction

CONTROL of grid-connected inverters, particularly under unbalanced and harmonically distorted grid voltages, is a crucial issue in operation of distributed generation (DG) systems. This is due to the fact that adverse grid voltage may distort the inverter injected current, which often leads to higher level of distortion current [1]–[3]. Recently, many control approaches, which focus on the performance of phase-locked loop and the current controller, have been proposed to minimize the total harmonic distortion (THD) level of injected current under such conditions.

In grid-connected inverter systems, a PLL is the most commonly used way of synchronizing DG systems with utility grid [4]. Under the normal grid condition, the phase angle of grid voltage can be obtained fast and precisely using the conventional synchronous reference frame PLL (SFR-PLL) [5]. However, the SRF-PLL is unable to detect the phase angle of grid voltage with a sufficient accuracy when the grid voltage is unbalanced and distorted [6]. One of the most effective approaches to enhance the robustness of the SFR-PLL is to incorporate the concept of a moving average filter (MAF) into PLL structure [6]–[8]. This additional feature enables the SRF-PLL to efficiently cancel out the effect of harmonics in the grid voltage on the detected phase angle. Though the MAF-based PLL has a reasonable steady-state response with low computational burden, its transient response is relatively slow. To overcome such a drawback, a MAF-PLL with a phase-lead compensator has been proposed [9]. By introducing a phase-lead compensator, the transient response of the MAF-PLL is significantly improved. However, as the transient response is improved, the steady-state performance is proportionally degraded in return.

In addition to PLL scheme, a current controller plays another important role in minimizing harmonic currents. Conventionally, a proportional integral (PI) controller or a proportional resonant (PR) controller is employed to control the injected current [10], [11]. However, the PI-based controller is inherently incapable of dealing with periodic disturbances efficiently. To overcome this limitation, different control approaches based on the resonant control, repetitive control, predictive control, and sliding mode control have been presented [12]–[24]. Among these approaches, incorporating resonant terms into the PR control structure to provide infinite gain at selected frequencies yields an excellent steady-state response even under distorted grid voltage [12]–[15]. This method, nevertheless, requires a great deal of computational efforts since one additional resonant controller is needed for each harmonic component. To reduce the number of resonant terms, the PI and resonant control (PI-RES) scheme has been studied [16], [17]. In these works, the resonant controller is implemented in the SRF in order that two harmonics are compensated at the same time. As a consequence, the number of resonant terms is reduced in half.

The main challenge of using high order linear controller is that it may be impractical to synthesize the controller that can fulfill both the stability and robustness requirements. Recently, robust current control schemes that can guarantee such requirements have been presented in [23] and [24]. In [24], the internal model of both the resonant controllers and inverter is lumped

Manuscript received December 30, 2016; revised May 1, 2017; accepted September 22, 2017. Date of publication September 26, 2017; date of current version May 17, 2018. This work was supported in part by the Basic Science Research Program through the National Research Foundation of Korea funded by the Ministry of Education (NRF-2016R1D1A1B03930975) and in part by the Human Resources Development of the Korea Institute of Energy Technology Evaluation and Planning grant funded by the Korea government Ministry of Trade, Industry & Energy (20154030200720). Paper no. TEC-01051-2016. *(Corresponding author: Kyeong-Hwa Kim.)*

The authors are with the Seoul National University of Science and Technology, Seoul 01811, South Korea (e-mail: laingocbao@gmail.com; k2h1@seoultech.ac.kr).

Color versions of one or more of the figures in this paper are available online at http://ieeexplore.ieee.org.

Digital Object Identifier 10.1109/TEC.2017.2757042

together. Then, the feedback and resonant gains can be obtained simultaneously by solving the linear matrix inequalities (LMIs) derived from the stability condition of the augmented system in Lyapunov sense. However, the control structure in [23] and [24] itself is not optimal in terms of computational burden as a result of implementing the controller in the stationary reference frame or natural frame. Moreover, the reported results show an unexpected transient response with a noticeable oscillation. Also, there was no numerical or practical evidence in these studies to prove the usefulness of this control method in the presence of adverse grid voltages. Another limitation of the work in [24] is that the current sensors both in inverter side and line side are required to accomplish the current controller. This often leads to the increase of cost and system complexity, especially in three-phase system.

In order to address the aforementioned limitations in existing research literatures regarding the control design procedure and system performance for grid-connected inverter, a robust control scheme for grid-connected inverters is presented in this paper. The proposed control scheme is achieved by a robust current control design and a MAF-based PLL method. The current controller is designed using the internal model (IM) principle and implemented in the SRF to ensure a good disturbance rejection capability with very low computation efforts. Moreover, all feedback gains are systematically obtained using the LMI optimization technique. Also, a state estimator is incorporated into the proposed control scheme to estimate the capacitor voltages and inverter currents. A simple and robust PLL scheme is introduced to enhance the dynamics of the SRF-PLL under adverse grid voltage. Simulations and experimental results under different grid conditions are given to demonstrate the effectiveness of the proposed control scheme.

II. System Description

To suppress the grid voltage disturbances due to imbalance and harmonic distortion, it is more effective to use the SRF rather than the stationary reference frame [17]. The transformation between *abc*- and *qd*-frame is done by means of Park's transformation [25]. Fig. 1 shows the proposed control scheme for a three-phase grid-connected inverter interfaced with the utility grid through an LCL filter. R_1, R_2, L_1, and L_2 represent the resistances and inductances of the filters, respectively, C_f represents the filter capacity, and L_g represents the grid inductance. The inverter is controlled by the proposed current controller through the space vector pulse width modulator (PWM) [26]. Also, the proposed PLL scheme is used to facilitate the grid synchronization. The proposed current controller and PLL scheme will be presented in detail in Section III. The continuous-time representation of the inverter can be expressed in the SRF which rotates synchronously with the angular speed of grid voltage ω_g as

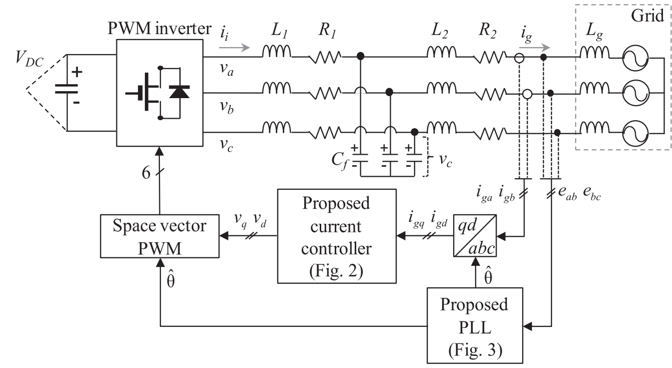

Fig. 1. Configuration of an LCL-filtered three-phase grid-connected inverter: power circuit and proposed control scheme.

$$\boldsymbol{x}_c(t) = \boldsymbol{A}_c\boldsymbol{x}_c(t) + \boldsymbol{B}_c\boldsymbol{u}_c(t) + \boldsymbol{B}_{cd}w_c(t) \tag{1}$$

$$\boldsymbol{y}(t) = \boldsymbol{C}_c\boldsymbol{x}_c(t) \tag{2}$$

where $\boldsymbol{x}_c = [\,i_{iq}\ i_{id}\ v_{cq}\ v_{cd}\ i_{gq}\ i_{gd}\,]^T$ with i_i, v_c, and i_g being the inverter current, capacitor voltage, and grid current, respectively, $\boldsymbol{u}_c = [\,v_q\ v_d\,]^T$ with v being the inverter output voltage, and $\boldsymbol{w}_c = [\,e_q\ e_d\,]^T$ with *e* being the grid voltage. The

$$\boldsymbol{A}_c = \begin{bmatrix} -R_1/L_1 & -\omega_g & 1/L_1 & 0 & 0 & 0 \\ \omega_g & -R_1/L_1 & 0 & 1/L_1 & 0 & 0 \\ 1/C_f & 0 & 0 & -\omega_g & -1/C_f & 0 \\ 0 & 1/C_f & \omega_g & 0 & 0 & -1/C_f \\ 0 & 0 & 1/L_f & 0 & -R_2/L_f & -\omega_g \\ 0 & 0 & 0 & 1/L_f & \omega_g & -R_2/L_f \end{bmatrix}$$

$$\boldsymbol{B}_c = \begin{bmatrix} 1/L_1 & 0 & 0 & 0 & 0 & 0 \\ 0 & 1/L_1 & 0 & 0 & 0 & 0 \end{bmatrix}^T,$$

$$\boldsymbol{C}_c = \begin{bmatrix} 0 & 0 & 0 & 0 & 1 & 0 \\ 0 & 0 & 0 & 0 & 0 & 1 \end{bmatrix},$$

$$\boldsymbol{B}_{cd} = \begin{bmatrix} 0 & 0 & 0 & 0 & -1/L_f & 0 \\ 0 & 0 & 0 & 0 & 0 & -1/L_f \end{bmatrix}^T.$$

subscripts q and d indicate that the designated quantity is in q-axis and d-axis of the SRF. In (1) and (2), the parametric matrices are expressed as the equation shown at the bottom of the previous page, where $L_f = L_2 + L_g$. For the purpose of digital realization, the system in (1) and (2) can be transformed into the discrete-time system which is facilitated by a zero-order hold with the sample period T_s as

$$\begin{bmatrix} \boldsymbol{x}_d(k+1) \\ \boldsymbol{\Phi}(k+1) \end{bmatrix} = \begin{bmatrix} \boldsymbol{A}_d & \boldsymbol{B}_d \\ \boldsymbol{0} & \boldsymbol{0} \end{bmatrix} \begin{bmatrix} \boldsymbol{x}_d(k) \\ \boldsymbol{\Phi}(k) \end{bmatrix} + \begin{bmatrix} \boldsymbol{0} \\ \boldsymbol{I} \end{bmatrix} \boldsymbol{u}(k) + \begin{bmatrix} \boldsymbol{B}_{dd} \\ \boldsymbol{0} \end{bmatrix} \boldsymbol{w}(k) \tag{3}$$

$$\boldsymbol{y}(k) = \begin{bmatrix} \boldsymbol{C}_c & \boldsymbol{0} \end{bmatrix} \begin{bmatrix} \boldsymbol{x}_d(k) \\ \boldsymbol{\Phi}(k) \end{bmatrix} \tag{4}$$

where $\boldsymbol{A}_d = e^{\boldsymbol{A}_c T_s}$, $\boldsymbol{B}_d = \int_0^{T_s} e^{\boldsymbol{A}_c \eta} d\eta \cdot \boldsymbol{B}_c$, $\boldsymbol{B}_{dd} = \int_0^{T_s} e^{\boldsymbol{A}_c \eta} d\eta \cdot \boldsymbol{B}_{cd}$, $\boldsymbol{0}$ and $\boldsymbol{I}$ denote zero and identity matrices with appropriate dimension, the variables $\boldsymbol{x}_d(k)$, $\boldsymbol{u}(k)$, and $\boldsymbol{w}(k)$ denote the discrete-time representation of $\boldsymbol{x}_c(t)$, $\boldsymbol{u}_c(t)$, and $\boldsymbol{w}_c(t)$, respectively, and the additional state vector $\boldsymbol{\Phi} \in \Re^{2\times 1}$ is introduced to model one sample period delay in the control input signal $\boldsymbol{u}$, which is due to the digital implementation [27].

The system in (3) and (4) can be rewritten in a compact form as

$$\boldsymbol{x}(k+1) = \boldsymbol{A}\boldsymbol{x}(k) + \boldsymbol{B}\boldsymbol{u}(k) + \boldsymbol{B}_d \boldsymbol{w}(k) \tag{5}$$

$$\boldsymbol{y}(k) = \boldsymbol{C}\boldsymbol{x}(k) \tag{6}$$

III. Proposed Control Scheme

The main objective of this section is to give complete guidance on designing the proposed robust control scheme that can cope with both the adverse grid voltage and the variation of grid impedance.

A. IM-Based Current Controller

According to [28] and [29], for unity feedback control system, an IM-based controller which ensures asymptotic reference tracking and disturbance rejection can be given in the continuous-time as

$$\dot{\boldsymbol{z}}_c(t) = \boldsymbol{H}_c \boldsymbol{z}_{ic}(t) + \boldsymbol{\Gamma}_{rc}\boldsymbol{r}(t) - \boldsymbol{\Gamma}_c \boldsymbol{C}_c \boldsymbol{x}_c(t) \tag{7}$$

$$\boldsymbol{u}(t) = \boldsymbol{K}_x \boldsymbol{x}_c(t) + \boldsymbol{K}_z \boldsymbol{z}_c(t) \tag{8}$$

where $\boldsymbol{z}_c = [\boldsymbol{z}_{Pc} \;\; \boldsymbol{z}_{2c} \;\; \boldsymbol{z}_{6c} \;\; \boldsymbol{z}_{12c}]^T$, $\boldsymbol{r} = [\boldsymbol{r}_P \;\; \boldsymbol{r}_2 \;\; \boldsymbol{r}_6 \;\; \boldsymbol{r}_{12}]^T$ being the reference vector, $\boldsymbol{K}_x, \boldsymbol{K}_z$ being the feedback gain matrices, and $\boldsymbol{H}_c, \boldsymbol{\Gamma}_c$ can be given as follows:

$$\boldsymbol{H}_c = \begin{bmatrix} \boldsymbol{H}_{Pc} & & & \\ & \boldsymbol{H}_{2c} & & \\ & & \boldsymbol{H}_{6c} & \\ & & & \boldsymbol{H}_{12c} \end{bmatrix},$$

$$\boldsymbol{\Gamma}_{rc} = \begin{bmatrix} \boldsymbol{\Gamma}_{Pc} & & & \\ & \boldsymbol{\Gamma}_{2c} & & \\ & & \boldsymbol{\Gamma}_{6c} & \\ & & & \boldsymbol{\Gamma}_{12c} \end{bmatrix}$$

and $\boldsymbol{\Gamma}_c = [\boldsymbol{\Gamma}_{Pc} \;\; \boldsymbol{\Gamma}_{2c} \;\; \boldsymbol{\Gamma}_{6c} \;\; \boldsymbol{\Gamma}_{12c}]^T$ where $\boldsymbol{H}_{Pc} = \boldsymbol{0}^{2\times 2}, \boldsymbol{\Gamma}_{Pc} = \boldsymbol{I}^{2\times 2}$,

$$\boldsymbol{H}_{ic} = \begin{bmatrix} 0 & 1 & 0 & 0 \\ -\omega_i^2 & 0 & 0 & 0 \\ 0 & 0 & 0 & 1 \\ 0 & 0 & -\omega_i^2 & 0 \end{bmatrix},$$

and

$$\boldsymbol{\Gamma}_{ic} = \begin{bmatrix} 0 & 0 \\ 1 & 0 \\ 0 & 0 \\ 0 & 1 \end{bmatrix} \text{ with } i = 2,\, 6,\, 12.$$

The controller in (7) and (8) is derived with the assumption that the grid voltage is unbalanced and polluted with 5th, 7th, 11th, and 13th harmonics. These sinusoidal disturbances have the angular frequency of 2nd, 6th, and 12th in the SRF. Moreover, the controller in (7) and (8) can be easily expanded for wider range of grid disturbance in the same manner. The discrete-time counterpart of (7) and (8) can be written as

$$\boldsymbol{z}(k+1) = \boldsymbol{H}\boldsymbol{z}(k) + \boldsymbol{\Gamma}_r \boldsymbol{r}(k) - \boldsymbol{\Gamma}\boldsymbol{C}\boldsymbol{x}(k) \tag{9}$$

$$\boldsymbol{u}(k) = \boldsymbol{K}_x \boldsymbol{x}(k) + \boldsymbol{K}_z \boldsymbol{z}(k) \tag{10}$$

where $\boldsymbol{H} = e^{\boldsymbol{H}_c T_s}$, $\boldsymbol{\Gamma}_r = \int_0^{T_s} e^{\boldsymbol{H}_c \eta} d\eta \cdot \boldsymbol{\Gamma}_{rc}$, and $\boldsymbol{\Gamma} = \int_0^{T_s} e^{\boldsymbol{H}_c \eta} d\eta \cdot \boldsymbol{\Gamma}_c$.

The existence of such controller is theoretically proved in [30] and [31].

B. Design of Robust and Optimal Feedback Gain

To determine a set of feedback gains that can guarantee the control performance as well as system stability, the inverter system in (5) and (6) is augmented with the controller in (9) and (10) as

$$\begin{bmatrix} \boldsymbol{x}(k+1) \\ \boldsymbol{z}(k+1) \end{bmatrix} = \begin{bmatrix} \boldsymbol{A} & \boldsymbol{0} \\ -\boldsymbol{\Gamma}\boldsymbol{C} & \boldsymbol{H} \end{bmatrix} \cdot \begin{bmatrix} \boldsymbol{x}(k) \\ \boldsymbol{z}(k) \end{bmatrix} + \begin{bmatrix} \boldsymbol{B} \\ \boldsymbol{0} \end{bmatrix} \boldsymbol{u}(k) + \begin{bmatrix} \boldsymbol{B}_d \\ \boldsymbol{0} \end{bmatrix} \boldsymbol{w}(k) + \begin{bmatrix} \boldsymbol{0} & \\ & \boldsymbol{\Gamma}_r \end{bmatrix} \boldsymbol{r}(k) \tag{11}$$

$$\boldsymbol{y}(k) = \begin{bmatrix} \boldsymbol{C} & \boldsymbol{0} \end{bmatrix} \begin{bmatrix} \boldsymbol{x}(k) \\ \boldsymbol{z}(k) \end{bmatrix} \tag{12}$$

$$\boldsymbol{u}(k) = \boldsymbol{K}_x \boldsymbol{x}(k) + \boldsymbol{K}_z \boldsymbol{z}(k) \tag{13}$$

The augmented system in (11)–(13) can be rewritten in a compact form as

$$\boldsymbol{\xi}(k+1) = \boldsymbol{A}_{\Sigma}\boldsymbol{\xi}(k) + \boldsymbol{B}_{\Sigma}\boldsymbol{u}(k) + \boldsymbol{B}_{d\Sigma}\boldsymbol{w}(k) + \boldsymbol{B}_{r\Sigma}\boldsymbol{r}(k) \tag{14}$$

$$\boldsymbol{y}(k) = \boldsymbol{C}_{\Sigma}\boldsymbol{\xi}(k) \tag{15}$$

$$\boldsymbol{u}(k) = \boldsymbol{K}\boldsymbol{\xi}(k) \tag{16}$$

where $\boldsymbol{K} = [\,\boldsymbol{K}_x \quad \boldsymbol{K}_z\,]$.

In practice, the grid impedance varies unpredictably. Even though the values of L_g are unknown, they are generally within a known bounded range. Then, according to [32], the system model in (14) can be written in a polytopic form as

$$\boldsymbol{\xi}(k+1) = \boldsymbol{A}_{\Sigma l}\boldsymbol{\xi}(k) + \boldsymbol{B}_{\Sigma l}\boldsymbol{u}(k) + \boldsymbol{B}_{d\Sigma l}\boldsymbol{w}(k) + \boldsymbol{B}_{r\Sigma l}\boldsymbol{r}(k) \tag{17}$$

where

$$(\boldsymbol{A}_{\Sigma}, \boldsymbol{B}_{\Sigma}, \boldsymbol{B}_{d\Sigma}, \boldsymbol{B}_{r\Sigma})(\alpha) = \sum_{l=1}^{2} \alpha_j (\boldsymbol{A}_{\Sigma}, \boldsymbol{B}_{\Sigma}, \boldsymbol{B}_{d\Sigma}, \boldsymbol{B}_{r\Sigma})_l$$

$$\sum_{l=1}^{2} \alpha_l = 1, \alpha_l \geq 0, l = 1, 2. \tag{18}$$

The vertex matrices in (18) are obtained by calculating the matrices $(\boldsymbol{A}_{\Sigma}, \boldsymbol{B}_{\Sigma}, \boldsymbol{B}_{d\sum}, \boldsymbol{B}_{r\sum})$ for the maximum and minimum values of grid inductance L_g.

Substituting (16) into (17) yields the closed-loop system as

$$\boldsymbol{\xi}(k+1) = (\boldsymbol{A}_{\Sigma l} + \boldsymbol{B}_{\Sigma l}\boldsymbol{K})\boldsymbol{\xi}(k) + \boldsymbol{B}_{d\Sigma l}\boldsymbol{w}(k) + \boldsymbol{B}_{r\Sigma l}\boldsymbol{r}(k) \tag{19}$$

$$\boldsymbol{y}(k) = \boldsymbol{C}_{\Sigma}\boldsymbol{\xi}(k) \tag{20}$$

From (19), it is able to derive the stability condition of the closed-loop system in the sense of Lyapunov as

$$(\boldsymbol{A}_{\Sigma l} + \boldsymbol{B}_{\Sigma l}\boldsymbol{K})^T \boldsymbol{P}(\boldsymbol{A}_{\Sigma l} + \boldsymbol{B}_{\Sigma l}\boldsymbol{K}) - \boldsymbol{P} < -(1-\varepsilon^2)\boldsymbol{P} \tag{21}$$

where ε $(0 < \varepsilon < 1)$ denotes the decay rate which represents the convergent rate of the system states, and $\boldsymbol{P} \in \Re^{22x22}$ is a positive definite matrix.

Applying Schur complement, (21) can be rewritten in a matrix form as

$$\begin{bmatrix} \varepsilon^2\boldsymbol{P} & (\boldsymbol{A}_{\Sigma l} + \boldsymbol{B}_{\Sigma l}\boldsymbol{K})^T \\ \boldsymbol{A}_{\Sigma l} + \boldsymbol{B}_{\Sigma\, l}\boldsymbol{K} & \boldsymbol{P}^{-1} \end{bmatrix} > 0. \tag{22}$$

Let us define $\boldsymbol{Q} = \boldsymbol{P}^{-1}$ and $\boldsymbol{Y} = \boldsymbol{K}\boldsymbol{Q}$. Then, the stability conditions of the augmented system can be written as

$$\begin{bmatrix} \varepsilon^2\boldsymbol{Q} & (\boldsymbol{A}_{\Sigma l}\boldsymbol{Q} + \boldsymbol{B}_{\Sigma l}\boldsymbol{Y})^T \\ \boldsymbol{A}_{\Sigma l}\boldsymbol{Q} + \boldsymbol{B}_{\Sigma l}\boldsymbol{Y} & \boldsymbol{Q} \end{bmatrix} > 0. \tag{23}$$

To minimize the control input with respect to a chosen decay rate ε, the feedback gain can be obtained by minimizing $\boldsymbol{Q}$ under the LMI constraints in (23) as

$$\underset{\varepsilon, \boldsymbol{Y}}{\text{Minimize}}\, \boldsymbol{Q} \text{ subject to } \quad (23) \tag{24}$$

As long as $\boldsymbol{Q}$ and $\boldsymbol{Y}$ are determined, the feedback gain matrix can be computed as $\boldsymbol{K} = \boldsymbol{Y}\boldsymbol{Q}^{-1}$.

It can be observed from (24) that all of the elements in the feedback gain matrix rely solely on the choice of the tunable scalar ε which guarantees the convergent speed of the Lyapunov function in (21). Therefore, the proposed design procedure simplifies the design of current controller. Also, for a chosen decay rate, all of the elements of $\boldsymbol{K}$ can be simultaneously obtained by solving (24), which accelerates the current controller design process. In order to select a proper decay rate, it would be useful to bear in mind that the decay rate in (24) is inversely proportional to the convergent rate of system states and directly proportional to the maximum tolerable value of grid impedance.

C. LMI-Based State Estimator

The controller in (9) and (10) is synthesized under the assumption that all the states are available for feedback. However, this is not often the case in three-phase LCL-filtered grid-connected inverter since the need for additional sensing devices brings about the increase in the overall cost and system complexity. Therefore, in this section, a LMI-based state estimator is introduced to estimate the system states which are i_c, v_c, and i_g from the control input and i_g.

From (3) and (4), the discrete-time representation of the LCL-filter which is not disturbed by the grid voltage and grid impedance can be given as

$$\boldsymbol{x}_d(k+1) = \boldsymbol{A}_d\boldsymbol{x}_d(k) + \boldsymbol{B}_d\boldsymbol{\Phi}(k) \tag{25}$$

$$\boldsymbol{y}(k) = \boldsymbol{C}_c\boldsymbol{x}_d(k). \tag{26}$$

According to [27], a state estimator can be constructed as

$$\tilde{\boldsymbol{x}}_d(k+1) = \boldsymbol{A}_d\tilde{\boldsymbol{x}}_d(k) + \boldsymbol{B}_d\boldsymbol{\Phi}(k) + \boldsymbol{L}(\boldsymbol{C}\tilde{\boldsymbol{x}}_d(k) - \boldsymbol{y}(k)) \tag{27}$$

where $\tilde{\boldsymbol{x}}_d \in \Re^{6\times 1}$ is the estimated state vector and $\boldsymbol{L} \in \Re^{6\times 2}$ is the estimator gain matrix.

In order to determine the value of $\boldsymbol{L}$, it is useful to obtain the estimation errors by subtracting (27) from (25) as

$$\tilde{\boldsymbol{x}}_e(k+1) = (\boldsymbol{A}_d + \boldsymbol{L}C)\tilde{\boldsymbol{x}}_e(k) \tag{28}$$

where $\tilde{\boldsymbol{x}}_e(k) = \boldsymbol{x}_d(k) - \tilde{\boldsymbol{x}}_d(k)$. Applying the same procedures in the previous subsection to (28), the LMI conditions for the state estimator can be obtained as

$$\begin{bmatrix} {\varepsilon_e}^2\boldsymbol{Q}_e & \boldsymbol{Q}_e\,\boldsymbol{A}_d + \boldsymbol{Y}_e\boldsymbol{C} \\ (\boldsymbol{Q}_e\,\boldsymbol{A}_d + \boldsymbol{Y}_e\boldsymbol{C})^T & \boldsymbol{Q}_e \end{bmatrix} > 0 \quad \text{and} \quad \boldsymbol{Q}_e > 0. \tag{29}$$

where $\boldsymbol{Q}_e \in \Re^{6\times 6}$ is a positive definite matrix, $\boldsymbol{Y}_e = \boldsymbol{Q}_e\,\boldsymbol{L}$, and $0 < \varepsilon_e < 1$ is the decay rate of the estimator. For a chosen decay rate, $\boldsymbol{Q}_e$ and $\boldsymbol{Y}_e$ can be obtained by solving the LMI optimization as follows:

$$\underset{\varepsilon_e, \boldsymbol{Y}_e}{\text{Minimize}}\, \boldsymbol{Q}_e \text{ subject to } \ (29), \tag{30}$$

then, the estimator gain matrix is evaluated as $\boldsymbol{L} = \boldsymbol{Q}_e^{-1}\,\boldsymbol{Y}_e$.

The block diagram of the proposed current controller is depicted in Fig. 2, where $\boldsymbol{\Gamma}_P$, $\boldsymbol{\Gamma}_2$, $\boldsymbol{\Gamma}_6$, $\boldsymbol{\Gamma}_{12}$, $\boldsymbol{H}_P$, $\boldsymbol{H}_2$, $\boldsymbol{H}_6$, and

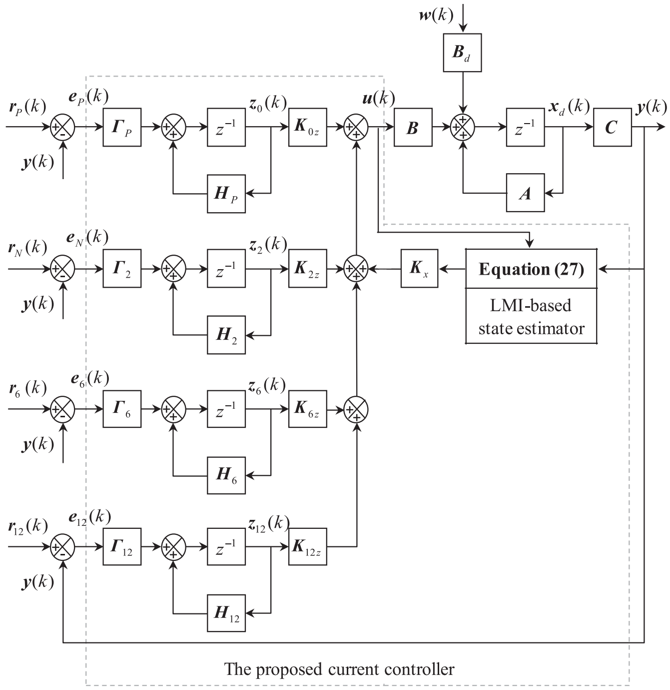

Fig. 2. Block diagram of the proposed current controller.

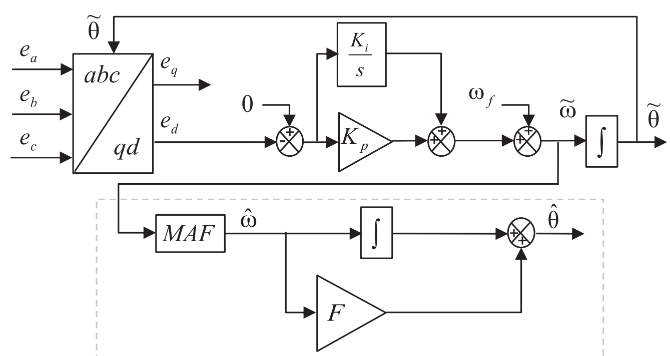

Fig. 3. Block diagram of the proposed PLL scheme.

$\boldsymbol{H}_{12}$ denote the discrete-time counterparts of $\boldsymbol{\Gamma}_{Pc}$, $\boldsymbol{\Gamma}_{2c}$, $\boldsymbol{\Gamma}_{6c}$, $\boldsymbol{\Gamma}_{12c}$, $\boldsymbol{H}_{Pc}$, $\boldsymbol{H}_{2c}$, $\boldsymbol{H}_{6c}$, and $\boldsymbol{H}_{12c}$, respectively.

D. Robust Grid Synchronization

To alleviate the adverse effect of grid disturbances on the detected grid angular frequency, a MAF concept is incorporated with the SRF-PLL scheme as shown in Fig. 3. Initially, the SRF-PLL is used to determine the grid angular frequency $\tilde{\omega}$ and angle $\tilde{\theta}$. After that, $\tilde{\omega}$ is processed by the MAF block to remove all the sinusoidal disturbances. The filtered angular frequency $\hat{\omega}$ is then used to construct the estimated phase angle $\hat{\theta}$. Unlike the MAF-PLL in [6], in the proposed PLL scheme, the MAF block locates outside of the closed-loop PLL to prevent any phase delay caused by the MAF on the dynamic characteristic of the SRF-PLL. Although placing the MAF outside of the SRF-PLL maintains the dynamic nature of the SRF-PLL, this introduces a consequential delay in $\hat{\omega}$ and $\hat{\theta}$. An adaptive delay compensator F is employed to compensate such a delay in $\hat{\theta}$ caused by the MAF. Since the implementation of the SRF-PLL and MAF has been clearly reported in [6], the remainder of this subsection is devoted to design the adaptive delay compensator F.

To design F, the discrete-time description of a MAF is taken into consideration as

$$\hat{\omega}(k) = \frac{1}{N} \sum_{i=0}^{N-1} \tilde{\omega}(k-i) \tag{31}$$

where N is the number of samples in a window length. The frequency response of the MAF can be calculated from (31) as

$$M(\omega) = \frac{1}{N} \sum_{i=0}^{N-1} e^{-j\omega T_w i} \tag{32}$$

where $T_w = NT_s$ is the window length of the MAF.

Applying the sum of a finite-length geometric series and Euler's formula to (32) yields the magnitude and phase as

$$M(\omega) = \frac{1}{N} \frac{(\sin(\omega T_s N/2)}{(\sin(\omega T_s/2))} e^{-j\omega T_s (N-1)/2}. \tag{33}$$

From (33), it is obvious that the MAF introduces a phase lag of $\omega T_s(N-1)/2$ into the filtered angular frequency $\hat{\omega}$, where the frequency ω in (33) is also the estimated grid frequency $\hat{\omega}$. Thus, the phase lag caused by the MAF can be written as $\hat{\omega} T_s(N-1)/2$. In order to remove such a phase lag completely, the estimated grid angle should be compensated by a phase lead of $+\hat{\omega} T_s(N-1)/2$. The block diagram of the delay compensator is also given in Fig. 3, where F is expressed as

$$F = \frac{T_s(N-1)}{2}. \tag{34}$$

IV. Simulation and Experimental Results

In order to highlight the superior performance of the proposed control scheme, the simulation using PSIM software and experiments have been carried out. The experimental system consists of a DSP based controller, a three-phase inverter with LCL filter, a transformer, and magnetic contactor for grid-connecting operation. The controller is implemented using a 32-bit floating-point DSP TMS320F28335 with the clock frequency of 150 MHz. The sampling period is chosen as 100 μsec, which yields the switching frequency of 10 kHz. A three-phase programmable AC power source (PACIFIC Power Source 320-ASX) is used to emulate various grid conditions. The parameters of a grid-connected inverter system are summarized as in Table I.

From Table I, $\boldsymbol{A}_{\Sigma l}$ and $\boldsymbol{B}_{\Sigma l}$ are evaluated for the maximum and minimum values of L_g. The decay rate of the current controller and the estimator are chosen to be $\varepsilon = 0.95$ and $\varepsilon_e = 0.85$, respectively. Then, $\boldsymbol{Q}$, $\boldsymbol{Y}$, $\boldsymbol{Q}_e$, and $\boldsymbol{Y}_e$ are calculated by solving the LMI optimization conditions in (24) and (30), respectively After that, the gains are computed as $\boldsymbol{K} = \boldsymbol{Y}\boldsymbol{Q}^{-1}$ and $\boldsymbol{L} = \boldsymbol{Q}_e^{-1}\boldsymbol{Y}_e$. In this paper, (24) and (30) are solved by LMI Control Toolbox in MATLAB [33].

Frequency responses of the closed-loop system using the proposed controller are given in Fig. 4. These responses clearly show that the closed-loop system has unity gain and zero phase

TABLE I
PARAMETERS OF GRID-CONNECTED INVERTER SYSTEM

Inverter nominal power: P		2.5	kW
Grid nominal frequency: f_g		60	Hz
Grid nominal line-line voltage		220	V
DC-link voltage: V_{DC}		340	V
Filter resistance: R_1/R_2		0.5/0.3 $\pm$ 10%	Ω
Filter inductance: L_1/L_2		1.7/0.6 $\pm$ 10%	mH
Filter capacitance: C_f		4.5 $\pm$ 10%	μF
Grid inductance: L_g	Min.	0	mH
	Max.	1.2	

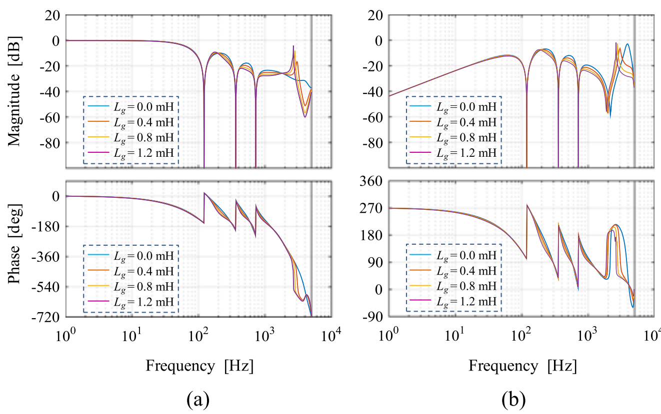

Fig. 4. Frequency responses of the closed-loop system using the proposed current controller under different values of L_g: (a) Reference tracking characteristic; (b) Disturbance rejection characteristic.

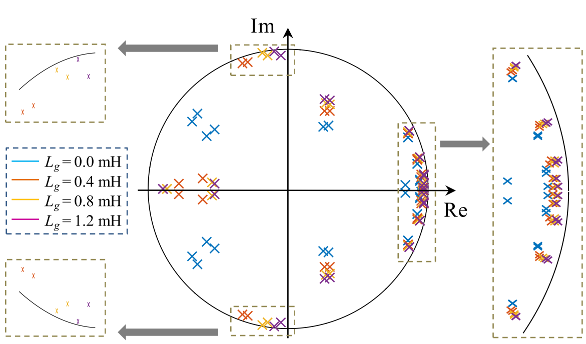

Fig. 5. Eigenvalues of the closed-loop system using the proposed current controller under different values of L_g.

at positive-sequence frequency, while very low gains at harmonic frequencies. This guarantees a good reference tracking and disturbance rejection characteristic as expected.

Fig. 5 shows the eigenvalues of the closed-loop system. The figure clearly demonstrates that some eigenvalues of the closed-loop system move towards the boundary of the unit circle, as the grid impedance increases. This movement indicates that the stability margin of the closed-loop system is reduced in accordance with the increase of gird impedance. Despite the variation of grid impedance, however, all the eigenvalues still remain inside the unit circle. This confirms the robustness of the proposed controller against parameter variations.

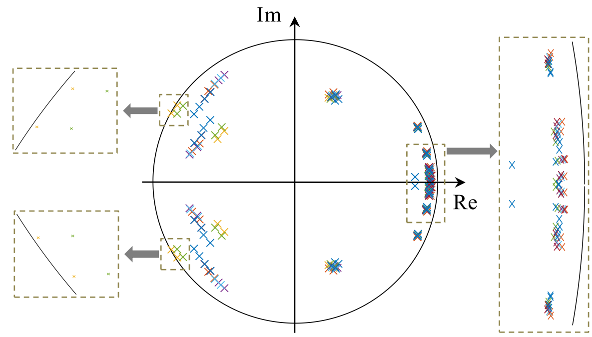

Fig. 6. Eigenvalues of closed-loop system using proposed current controller under parameter variations of R_1, R_2, L_g, L_2 and C_f.

In designing the proposed current controller, the perturbation of filter parameters such as R_1, R_2, L_1, L_2, and C_f are not considered since these parameters are subject to only small variations during operation. Nevertheless, the designed controller should be capable of tolerating the variations of such parameters. To investigate the system stability under the perturbation of such filter parameters, Fig. 6 represents the plots of eigenvalues of the inverter system when L_1, R_1, R_2, L_f, and C_f are varied with $\pm 10\%$ from the nominal values. From Fig. 6, it is clearly seen that all the eigenvalues lie in the unit circle despite the variations of these inverter parameters. This well verifies the robustness of the proposed controller against filter parameter variations.

To highlight the robustness of the proposed control scheme against adverse grid voltage, two different grid conditions are used. One is the ideal grid voltage whose harmonic contents are negligibly low. The other is three-phase unbalanced and distorted grid voltages which have 80% voltage sag in *c*-phase and contain the 5th, the 7th, the 11th, and the 13th harmonic components with the magnitude of 10%, 10%, 5%, and 5% with respect to *a*-phase voltage, which yields the THD value of 15.8%.

Fig. 7 shows the simulation results of three PLL schemes when the grid voltage undergoes a step change in frequency by +5 Hz. It can be observed that the dynamic response of the proposed PLL scheme is as good as that of the SRF-PLL. On the other hand, the conventional MAF-PLL scheme suffers a slow transient response. Moreover, in Fig. 7(b), the SRF-PLL exhibits large oscillation in detected frequency due to poor filtering capability in comparison to the MAF-PLL and the proposed PLL schemes. Also, the proposed PLL scheme has the lowest value of steady-state errors under the ideal as well as abnormal grid conditions. These results imply that the proposed PLL scheme offers preferable dynamic and steady-state response.

To verify the effectiveness of the proposed control scheme, the performance is compared with the PI-RES controller [17] and an extended version of the controller in [24]. The transfer function of a PI-RES controller is given in the SRF as

$$G_{PI+RES} = K_p + \frac{K_i}{s} + \frac{2 \cdot K_{r2} \cdot s}{s^2 + (2\omega_g)^2} + \frac{2 \cdot K_{r6} \cdot s}{s^2 + (6\omega_g)^2} + \frac{2 \cdot K_{r12} \cdot s}{s^2 + (12\omega_g)^2}.$$

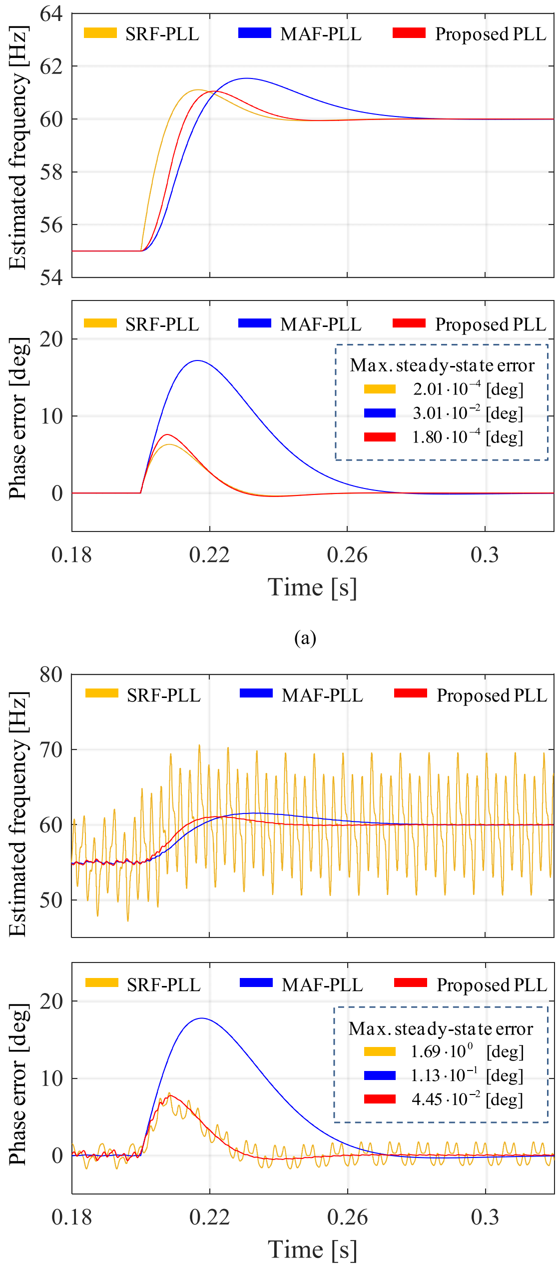

Fig. 7. Simulation results when the grid voltage undergoes a step change in frequency by +5 Hz: (a) Under the ideal grid voltage; (b) Under unbalanced and distorted grid voltage.

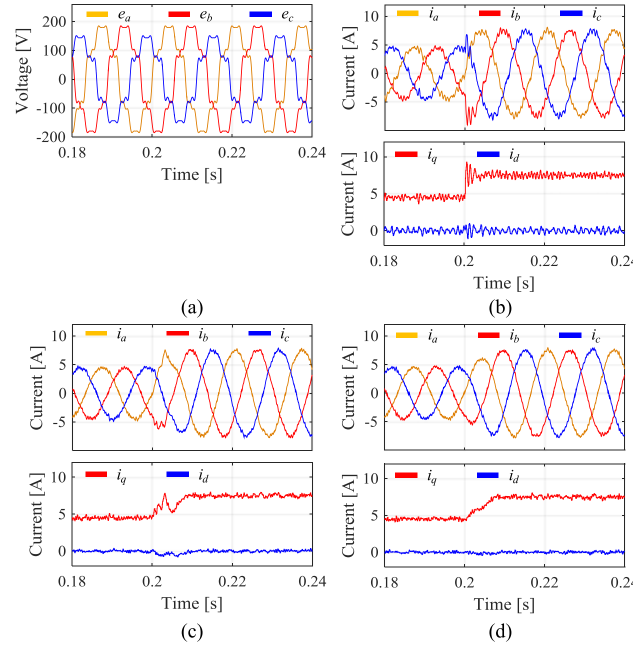

Fig. 8. Simulation results of transient response under unbalanced and distorted grid voltages: (a) Three-phase unbalanced and distorted grid voltages; (b) PI-RES controller with the SRF-PLL; (c) Extended controller of [24] with the SRF-PLL; (d) Proposed control scheme.

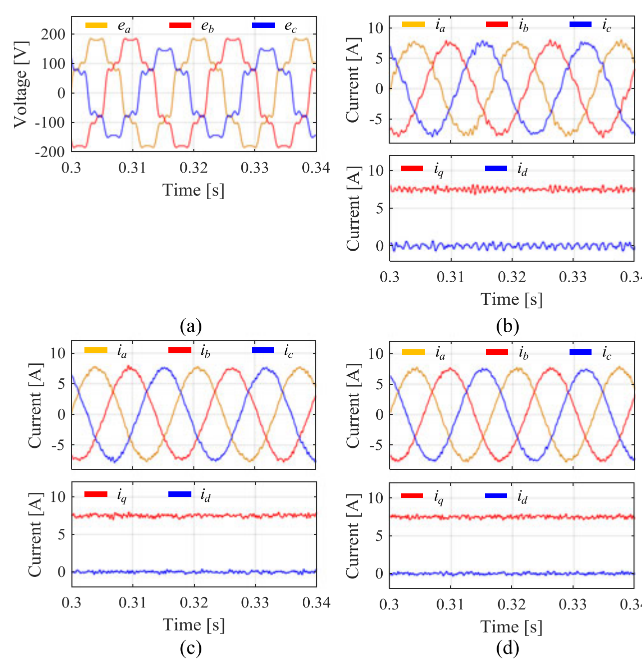

Fig. 9. Simulation results under unbalanced and distorted grid voltages: (a) Three-phase unbalanced and distorted grid voltages; (b) PI-RES controller with the SRF-PLL; (c) Extended controller of [24] with the SRF-PLL; (d) Proposed control scheme.

where $K_p = 18$, $K_i = 8000$, $K_{r2} = 8000$, $K_{r6} = 8000$, and $K_{r12} = 8000$. Also, the controller in [24] was especially presented for a single-phase inverter and only applicable for LCL-filtered inverter when the full information of system states is available. However, the grid-connected inverter described in Fig. 1 is three-phase and has only the information on grid voltage and grid current. Therefore, the controller in [24] is extended to be applicable to such a system and comparable with the propose control scheme. For this purpose, the extended controller of [24] is implemented in the SRF and incorporated with the state estimator as in Section III-C. Also, both the PI-RES controller and the extended controller of [24] are synchronized with the grid using the SRF-PLL.

Figs. 8 and 9 show the simulation results under unbalanced and distorted grid voltages using three control schemes. As can be observed, under a step change of q-axis reference current of 3 A, the settling time for three control schemes is more or

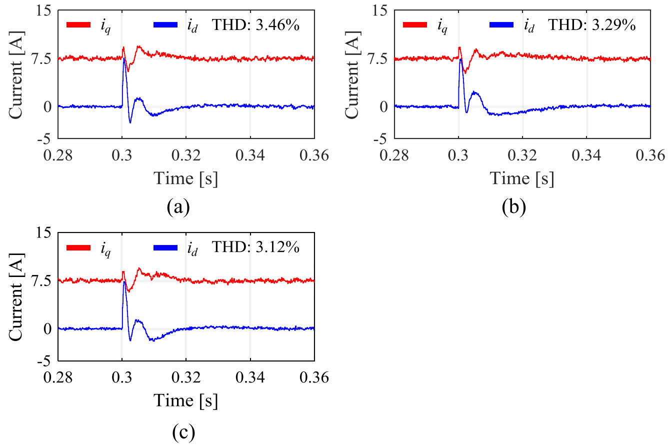

Fig. 10. Responses of the proposed current controller to a $+10°$ phase angle transition of unbalanced and distorted grid voltage: (a) with SRF-PLL; (b) with MAF-PLL; (c) with proposed PLL.

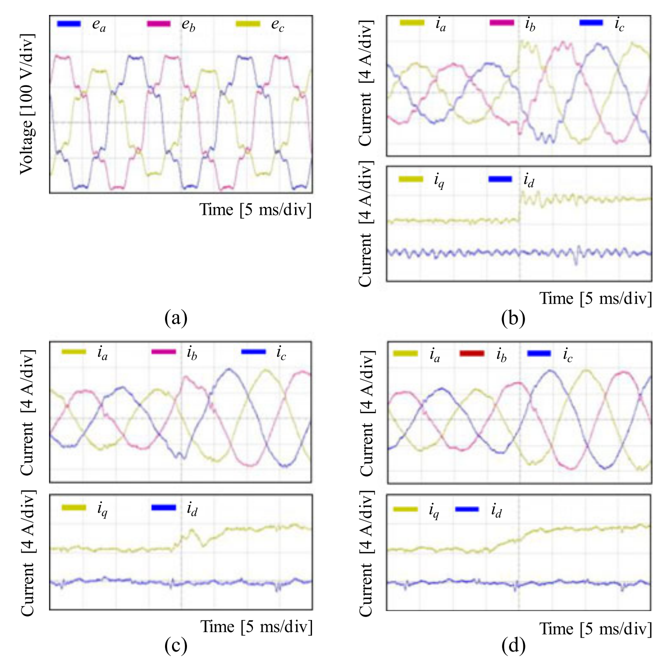

Fig. 11. Experimental results of transient response under unbalanced and distorted grid voltages: (a) actual unbalanced and distorted grid voltage; (b) PI-RES controller with the SRF-PLL; (c) extended controller of [24] with the SRF-PLL; (d) proposed control scheme.

less the same with 10 msec. Nevertheless, the PI-RES controller with the SRF-PLL, and the extended controller of [24] with the SRF-PLL suffer severe oscillation during transient periods, which may lead to the degradation of grid power quality as well as ineffective use of primary power sources. Also, as is clearly shown in Fig. 9, the proposed control scheme offers the highest quality of injected currents.

To investigate the influence of the proposed PLL scheme on the current control, Fig. 10 shows the simulation results for current responses when three PLL schemes are applied to the proposed current controller under $+10°$ phase angle transition of unbalanced and distorted grid voltage. As is shown in Fig. 10(c), the proposed PLL scheme gives the lowest THD

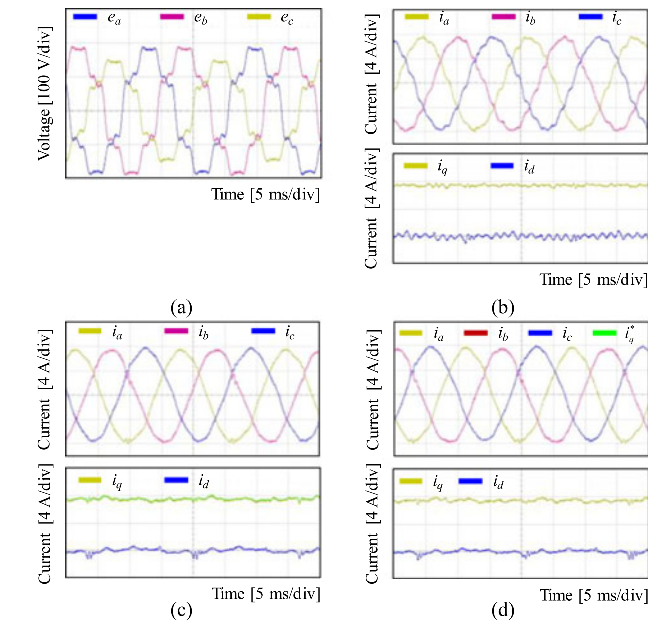

Fig. 12. Experimental results under unbalanced and distorted grid voltages: (a) Actual unbalanced and distorted grid voltage; (b) PI-RES controller with the SRF-PLL; (c) Extended controller of [24] with the SRF-PLL; (d) Proposed control scheme.

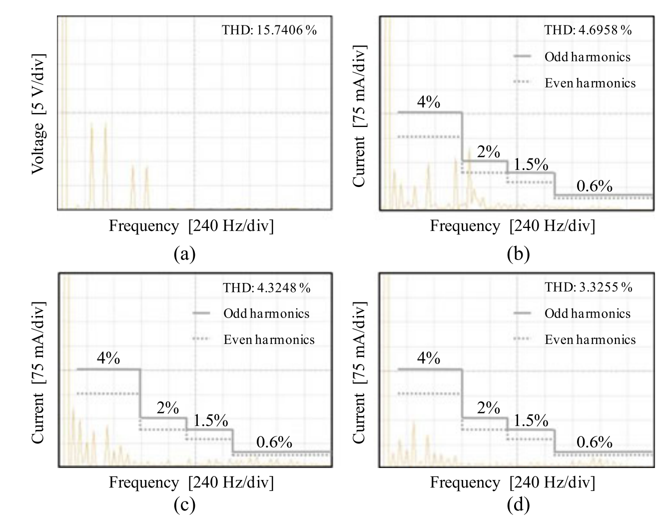

Fig. 13. Experimental FFT results of *a*-phase current in comparison with IEEE Std. 1547: (a) Actual unbalanced and distorted grid voltage; (b) PI-RES controller with the SRF-PLL; (c) Extended controller of [24] with the SRF-PLL; (d) Proposed control scheme.

value in currents. Even though the difference in dynamic response of currents is not significant due to robust characteristic of the proposed current controller providing a good dynamic performance, a slight dynamic improvement is still observed in Fig. 10(c) as compared with Fig. 10(b).

To validate the usefulness of the proposed control scheme in view of the practical aspect, the experimental results corresponding to those in Figs. 8 and 9 are given in Figs. 11 and 12. From these results, it is confirmed that the experimental results correspond well with the simulations. As a result, the proposed control scheme offers better steady-state and dynamic responses than the existing control approaches.

To evaluate the injected current quality, the experimental FFT results of *a*-phase current under unbalanced and distorted grid voltage are shown in Fig. 13. Also, the harmonic limit according to IEEE Std. 1547 is given in these figures. Fig. 13(a) shows the FFT data and THD value of *a*-phase grid voltage. As is shown in Fig. 13(b), under such a heavily distorted grid voltage, the PI-RES controller with the SRF-PLL fails to meet the grid interconnection requirements in terms of injected current quality. On the other hand, both extended controller of [24] with the SRF-PLL and the proposed control scheme satisfy the standard. Nevertheless, the proposed control scheme gives the smaller THD level of 3.3255% in comparison to 4.3248% in the case of extended controller of [24] with the SRF-PLL.

V. Conclusion

In this paper, a robust control scheme for grid-connected inverters with LCL filter under unbalanced and distorted grid conditions has been presented. The proposed control scheme is primarily achieved by an IM-based current controller and a robust PLL scheme. The key component of the proposed scheme is a design of IM-based current controller where the gains are systematically obtained for a chosen decay rate by adopting the LMI optimization approach. The LMI optimization approach is also employed to design a state estimator. The proposed scheme ensures harmonic-free injected currents and smooth transient response even under severely abnormal grid voltages. In addition, a great deal of computational efforts is reduced as a result of implementing the controller in the SRF. Also, a simple and robust PLL scheme has been proposed in this paper to detect the angular frequency of fundamental grid voltage fast and precisely. This can contribute to improve the performance of grid-connected inverter systems in view of effectiveness and secure operation. The simulation and experimental results well confirmed the performance improvements in both transient and steady-state operations even in the presence of harsh grid environment.

References

[1] A. M. Bouzid, J. M. Guerrero, A. Cheriti, M. Bouhamida, P. Sicard, and M. Benghanem, “A survey on control of electric power distributed generation systems for microgrid applications,” *Renew. Sustain. Energy Rev.*, vol. 44, pp. 751–766, Apr. 2015.

[2] I. Patrao, E. Figueres, G. Garcera, and R. Gonzalez-Medina, “Microgrid architectures for low voltage distributed generation,” *Renew. Sustain. Energy Rev.*, vol. 43, pp. 415–422, Mar. 2015.

[3] *Standard for Interconnecting Distributed Resources With Electric Power Systems*, IEEE Std. 1547-2003, Jun. 2003.

[4] S. Chung, “A phase tracking system for three phase utility interface inverters,” *IEEE Trans. Power Electron.*, vol. 15, no. 3, pp. 431–438, May 2000.

[5] F. Blaabjerg, R. Teodorescu, M. Liserre, and A. V. Timbus, “Overview of control and grid synchronization for distributed power generation systems,” *IEEE Trans. Ind. Electron.*, vol. 53, no. 5, pp. 1398–1409, Oct. 2006.

[6] S. Golestan, M. Ramezani, J. M. Guerrero, F. D. Freijedo, and M. Monfared, “Moving average filter based phase-locked loops: Performance analysis and design guidelines,” *IEEE Trans. Power Electron.*, vol. 29, no. 6, pp. 2750–2763, Jun. 2014.

[7] E. Robles, S. Ceballos, J. Pou, J. L. Martin, J. Zaragoza, and P. Ibanez, “Variable-frequency grid-sequence detector based on a quasi-ideal low-pass filter stage and a phase-locked loop,” *IEEE Trans. Power Electron.*, vol. 25, no. 10, pp. 2552–2563, Oct. 2010.

[8] F. Freijedo, J. Doval-Gandoy, O. Lopez, and E. Acha, “A generic open-loop algorithm for three-phase grid voltage/current synchronization with particular reference to phase, frequency, and amplitude estimation,” *IEEE Trans. Power Electron.*, vol. 24, no. 1, pp. 94–107, Jan. 2009.

[9] S. Golestan, J. M. Guerrero, and A. M. Abusorrah, “MAF-PLL with phase-lead compensator,” *IEEE Trans. Ind. Electron.*, vol. 62, no. 6, pp. 3691–3695, Jun. 2015.

[10] Z. Yao, L. Xiao, and J. M. Guerrero, “Improved control strategy for the three-phase grid-connected inverter,” *IET Renew. Power Gener.*, vol. 9, no. 6, pp. 587–592, Jan. 2015.

[11] D. N. Zmood and D. G. Holmes, “Stationary frame current regulation of PWM inverters with zero steady-state error,” *IEEE Trans. Power Electron.*, vol. 18, no. 3, pp. 814–822, May 2003.

[12] J. C. Vasquez, J. M. Guerrero, M. Savaghebi, J. Eloy-Garcia, and R. Teodorescu, “Modeling, analysis, and design of stationary-reference-frame droop-controlled parallel three-phase voltage source inverters,” *IEEE Trans. Ind. Electron.*, vol. 60, no. 4, pp. 1271–1280, Apr. 2013.

[13] R. Teodorescu, F. Blaabjerg, M. Liserre, and P. C. Loh, “Proportional-resonant controllers and filters for grid-connected voltage-source converters,” *Inst. Electr. Eng. Proc., Electr. Power Appl.*, vol. 153, no. 5, pp. 750–762, Sep. 2006.

[14] M. Castilla, J. Miret, A. Camacho, J. Matas, and L. G. de Vicuña, “Reduction of current harmonic distortion in three-phase grid-connected photovoltaic inverters via resonant current control,” *IEEE Trans. Ind. Electron.*, vol. 60, no. 4, pp. 1464–1472, Apr. 2013.

[15] X. Yuan, W. Merk, H. Stemmler, and J. Allmeling, “Stationary-frame generalized integrators for current control of active power filters with zero steady-state error for current harmonics of concern under unbalanced and distorted operating conditions,” *IEEE Trans. Ind. Appl.*, vol. 38, no. 2, pp. 523–532, Mar. 2002.

[16] M. Liserre, R. Teodorescu, and F. Blaabjerg, “Multiple harmonics control for three-phase grid converters systems with the use of PI-RES current controller in a rotating frame,” *IEEE Trans. Power Electron.*, vol. 21, no. 3, pp. 836–841, May 2006.

[17] R. I. Bojoi, G. Griva, V. Bostan, M. Guerriero, F. Farina, and F. Profumo, “Current control strategy for power conditioners using sinusoidal signal integrators in synchronous reference frame,” *IEEE Trans. Power Electron.*, vol. 20, no. 6, pp. 1402–1412, Nov. 2005.

[18] S. W. Kang and K. H. Kim, “Sliding mode harmonic compensation strategy for power quality improvement of a grid-connected inverter under distorted grid condition,” *IET Power Electron.*, vol. 8, no. 8, pp. 1461–1472, Feb. 2015.

[19] Q. C. Zhong and T. Hornik, “Cascaded current-voltage control to improve the power quality for a grid-connected inverter with a local load,” *IEEE Trans. Ind. Electron.*, vol. 60, no. 4, pp. 1344–1355, Apr. 2013.

[20] Y. Jia, J. Zhao, and X. Fu, “Direct grid current control of *LCL*-filtered grid-connected inverter mitigating grid voltage disturbance,” *IEEE Trans. Power Electron.*, vol. 29, no. 3, pp. 1532–1541, Mar. 2014.

[21] Y. A. I. Mohamed, “Mitigating of dynamic, unbalanced, and harmonic voltage disturbance using grid-connected inverters with *LCL* filter,” *IEEE Trans. Ind. Electron.*, vol. 58, no. 9, pp. 3914–3924, Sep. 2011.

[22] J. R. Fischer, S. A. Gonzalez, I. Carugati, M. A. Herran, M. G. Judewicz, and D. O. Carrica, “Robust predictive control of grid-tied converters based on direct power control,” *IEEE Trans. Power Electron.*, vol. 29, no. 10, pp. 5634–5643, Oct. 2014.

[23] I. J. Gabe, V. F. Montagner, and H. Pinheiro, “Design and implementation of a robust current controller for VSI connected to the grid through an *LCL* filter,” *IEEE Trans. Power Electron.*, vol. 24, no. 6, pp. 1444–1452, Jun. 2009.

[24] L. A. Maccari *et al.*, “LMI-based control for grid-connected converters with *LCL* filters under uncertain parameters,” *IEEE Trans. Power Electron.*, vol. 29, no. 7, pp. 3776–3785, Jul. 2014.

[25] P. C. Krause, O. Wasynczuk, and S. D. Sudhoff, *Analysis of Electric Machinery and Drive Systems*, 2nd ed. Piscataway, NJ, USA: IEEE Press, 2002.

[26] M. P. Kazmierkowski, F. Blaabjerg, and R. Krishnan, *Control in Power Electronics; Selected Problems*, London, U.K.: Academic, 2002.

[27] G. F. Franklin, J. D. Powell, and M. Workman, *Digital Control of Dynamic Systems*, 3rd ed. Petaluma, CA, USA: Addison-Wesley Longman, 1998.

[28] B. A. Francis and W. M. Wonham, “The internal model principle of control theory,” *Automatica*, vol. 12, no. 5, pp. 475–465, Sep. 1976.

[29] G. F. Franklin, J. D. Powell, and A. Emami-Naeini, *Feedback Control of Dynamic Systems*, 7th ed. Upper Saddle River, NJ, USA: Pearson Higher Education Inc., 2015.

[30] C. Chen, *Linear System Theory and Design*, 4th ed. New York, NY, USA: Oxford Univ. Press, 2013.
[31] J. Huang, *Nonlinear Output Regulation Theory and Application*. Philadelphia, PA, USA: SIAM, 2004.
[32] S. Boyd, L. EL Ghaoui, E. Feron, and V. Balakrishnan, *Linear Matrix Inequalities in System and Control Theory*. Philadelphia, PA, USA: SIAM, 1994.
[33] P. Gahinet, A. menirovskii, A. J. Laub, and M. Chilali, *LMI Control Toolbox User's Guide*. Natick, MA, USA: Math Works, 1995.

Ngoc-Bao Lai was born in Thanh Hoa, Vietnam, in 1991. He received the B.S. degree in electrical engineering from Danang University of Science and Technology, Da Nang, Vietnam, in 2014, and the M.S. degree in 2017 in electrical and information engineering from Seoul National University of Science and Technology, Seoul, South Korea, where he is currently working toward the Ph.D. degree. His research interests include robust control, power electronics, distributed generation systems, and microgrid.

Kyeong-Hwa Kim (M'13) was born in Seoul, South Korea, in 1969. He received the B.S. degree from Hanyang University, Seoul, South Korea, in 1991, and the M.S. and Ph.D. degrees from Korea Advanced Institute of Science and Technology (KAIST), Daejeon, South Korea, in 1993 and 1998, respectively, all in electrical engineering. From 1998 to 2000, he was a Research Engineer with Samsung Electronics Company, South Korea, where he was engaged in the research and development of ac machine drive systems. From 2000 to 2002, he was a Research Professor with KAIST. From August 2010 to August 2011, he was a Visiting Scholar with the Virginia Polytechnic Institute and State University (Virginia Tech), Blacksburg, VA, USA. Since August 2002, he has been with the Seoul National University of Science and Technology, Seoul, where he is currently working as a Professor. His current research interests include ac machine drives, the control and diagnosis of power systems, power electronics, renewable energy, and DSP-based control applications. He is a member of the Korean Institute of Power Electronics.